Materials Advances

ROYAL SOCIETY OF CHEMISTRY

PAPER

View Article Online
View Journal | View Issue

Check for updates

Cite this: *Mater. Adv.*, 2022, 3, 6246

Received 7th June 2022,
Accepted 18th June 2022

DOI: 10.1039/d2ma00653g

rsc.li/materials-advances

Transition metal sulfide/hydroxide electrode materials with high specific capacities

Tong Xia,[a] Ahmad Umar[b] and Xiang Wu *[a]

Nowadays, research on energy storage devices is mainly focused on enhancing their electrochemical performance. Among them, electrode materials play an important role. In this work, we synthesised several hybrid $NiCo_2S_4$@$Ni(OH)_2$ samples by a three-step hydrothermal route. As electrode materials, the obtained flower-like structures can accelerate the transfer of electrolyte ions. They possess a specific capacity of 2899.48 F g^{-1} at 1 A g^{-1} and superior cycle stability. Moreover, the assembled hybrid device obtains an energy density of 59.26 W h kg^{-1} at 1432.07 W kg^{-1}. Bending tests at different angles indicate that the device possesses excellent mechanical flexibility.

1. Introduction

At present, the demand for clean energy resources has become overwhelming due to superfluous carbon emission.[1–3] As an emerging energy storage device, a supercapacitor not only fills the gap between traditional capacitors and batteries, but also shows many advantages, such as a wide working temperature range and long cycle life.[4–6] However, its relatively low energy density hinders its further application.[7,8] It is known that increasing the specific capacitance (C) and voltage window (V) can improve the corresponding energy density.[9–11] Transition metal sulfides have been extensively studied for their excellent electrochemical activity and ultra-high redox capacity.[12–14] For example, Ma *et al.* fabricated $NiCo_2S_4$ electrode materials on carbon nanofibers by electrospinning and hydrothermal methods. The prepared samples showed a mass capacitance of 1169 F g^{-1} at 1 A g^{-1}. The capacitance retention rate was 87.2% after 10 000 cycles.[15] In previous work, we prepared $NiCo_2S_4$ nanowires using a two-step hydrothermal route. The resulting product possessed a specific capacitance of 1382.44 C g^{-1} at 1 A g^{-1}.[16] Nickel hydroxide is also widely used in supercapacitors because of its high theoretical capacitance and unique layer structure.[17–19] Sharif's group prepared $Co(OH)_2$@$Ni(OH)_2$ nanosheets on 3D-Ni film-coated nickel wires by an electrochemical route. They delivered a specific capacitance of 355.2 C g^{-1} at 1 A g^{-1} and 80.0% capacitance retention after 3000 cycles.[20]

However, single-component materials often show poor conductivity.[21] This limits the full utilization of their electrochemical performance. The construction of heterogeneously structured electrode materials is an efficient strategy to increase their specific capacitance. The increase in electrical conductivity of the electrode material can be achieved by using the synergistic effect of multiple components. The unique structure facilitates the transport of electrolyte ions, resulting in an increase in specific capacitance.[22,23] For instance, Li and coworkers prepared $NiCo_2S_4$@PPy composite material on Ni foam by hydrothermal and *in situ* polymerization methods. The obtained samples achieved a capacitance of 1842.8 F g^{-1} (at 1 A g^{-1}). The energy density of the prepared hybrid device was 41.2 W h kg^{-1} at 402.2 W kg^{-1} and the capacitance retention rate obtained was as high as 92.8%.[24] Sekar *et al.* synthesized $NiCo_2S_4$@C_3N_4@VS_2 nanocomposites through a multi-step hydrothermal approach. It showed a specific capacity of 1984.1 F g^{-1} at 1 A g^{-1}.[25]

In this work, we report hybrid $NiCo_2S_4$@$Ni(OH)_2$ electrode materials on Ni foam by a multi-step hydrothermal approach. The mass capacitance of the prepared sample is 2899.48 F g^{-1} at 1 A g^{-1}. It shows an excellent cycling stability after 10 000 cycles charge/discharge tests and a capacitance retention rate of 85%. The assembled asymmetric device delivers an energy density of 59.26 W h kg^{-1} at 1432.07 W kg^{-1}. It also shows excellent mechanical flexibility at different bending angles.

2. Experimental

Preparation of $NiCo_2S_4$ nanosheets

In a typical procedure, 0.29 g of $Ni(NO_3)_2 \cdot 6H_2O$, 0.58 g of $Co(NO_3)_2 \cdot 6H_2O$, 0.11 g of NH_4F and 1.5 g of urea were added in turn to 60 mL of deionized water. Then a piece of pretreated nickel foam was put into the above mixed solution. After that, the reaction was carried out at 120 °C for 5 h. After cooling to room temperature, the

[a] School of Materials Science and Engineering, Shenyang University of Technology, Shenyang 110870, P. R. China. E-mail: wuxiang05@163.com, wuxiang05@sut.edu.cn
[b] Department of Chemistry, Najran University, Najran 11001, Kingdom of Saudi Arabia

resulting product was washed with deionized water and ethanol, consecutively, and then dried at 60 °C. Finally, 0.4 g of $Na_2S{\cdot}9H_2O$ and the above precursors were added to 60 mL of deionized water and then transferred to an autoclave and stored at 120 °C for 4 h. The average mass loading of $NiCo_2S_4$ was 1 mg cm^{-2}.

Synthesis of $NiCo_2S_4$@$Ni(OH)_2$ composite materials

0.29 g of $Ni(NO_3)_2{\cdot}6H_2O$ and 0.12 g of urea were put into 60 mL of deionized water with thorough stirring, and then the prepared $NiCo_2S_4$ sample was put into the above solution, and kept at 120 °C for 2 h. Several experiments were conducted with different reaction times (1, 2, 4 h). The samples were marked $NiCo_2S_4$@$Ni(OH)_2$-1, $NiCo_2S_4$@$Ni(OH)_2$-2 and $NiCo_2S_4$@$Ni(OH)_2$-4. Their average masses were 1, 1.1 and 1.7 mg cm^{-2}, respectively.

Preparation of activated carbon

Activated carbon, acetylene black and polyvinylidene fluoride were mixed in a ratio of 7 : 2 : 1 and a slurry was prepared with *N*-methyl-2-pyrrolidone. Afterwards, it was evenly coated on nickel foam and then dried.

Assembly of asymmetric supercapacitors

An $NiCo_2S_4$@$Ni(OH)_2$-2 positive electrode and activated carbon were used to assemble asymmetric supercapacitors. PVA-KOH was used as a gel electrolyte and a diaphragm (NKK paper) as a separator.

The active substance mass of electrode materials can be calculated according to the formula:

$$m^+/m^- = C^-\Delta V^-/(C^+\Delta V^+) \quad (1)$$

where m^+, m^- are the active substance masses of positive and negative electrodes, respectively, C^+, C^- are the mass capacitances, and ΔV^+, ΔV^- are the voltage windows.

Material characterization

The phase composition of the synthesised material was studied using an X-ray diffractometer (XRD, Shimadzu-7000, $\lambda = 0.1506$) containing Cu Kα radiation. X-ray photoelectron spectroscopy (XPS, ESCALAB 250 Xi, Thermo Scientific) was used to investigate the chemical valence of the products. The morphology of the samples could be observed with a scanning electron microscope (SEM; Gemini SEM 300-71-31) and a transmission electron microscope (TEM, JEM-2100 PLUS).

Electrochemical measurements

The electrochemical performance of the samples was examined in an electrochemical workstation (CHI600E, Chenhua, Shanghai). The synthetic samples, Hg/HgO (0.098 V) and Pt sheets were used as the three electrode materials. The test content mainly includes cyclic voltammetry, galvanostatic charge–discharge and electrochemical impedance spectroscopy.

3. Results and discussion

The preparation process of the $NiCo_2S_4$@$Ni(OH)_2$ samples is illustrated in Fig. 1. Firstly, $NiCo_2S_4$ nanosheets were synthesized

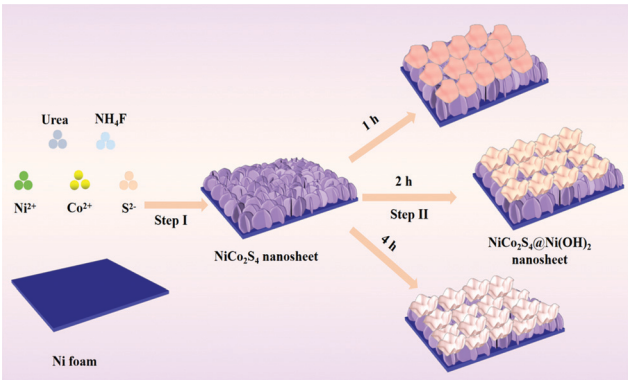

Fig. 1 The synthetic schematic of $NiCo_2S_4$@$Ni(OH)_2$ composites.

using a simple hydrothermal method. Then, a layer of $Ni(OH)_2$ nanosheets was covered on the surface of the $NiCo_2S_4$ product by a one-step hydrothermal route. When the reaction time increased, the composite $Ni(OH)_2$ nanosheets gradually assembled into nanoflower shapes. The two-layer nanosheet structure allows for a synergistic effect between the two materials. It significantly increases the electrochemically active sites and results in high specific capacitance.

The XRD patterns of the samples are shown in Fig. 2a. Three typical diffraction peaks come from the nickel substrate. The peak at 31.6° corresponds to the (311) crystal planes of $NiCo_2S_4$ (JCPDS no. 20-0782), while those at 38.3°, 50.5° and 69.3° are in accordance with the (400), (511), and (440) crystal planes, respectively. When it is composed with $Ni(OH)_2$ material, several additional diffraction peaks are detected at 38.5°, 59.1° and 73.1°, which belong to the (101), (110) and (112) crystal planes of $Ni(OH)_2$ (JCPDS no. 14-0117). The element surface states of $NiCo_2S_4$@$Ni(OH)_2$-2 were then studied by XPS. Ni 2p can be divided into two spin orbitals of Ni^{2+} and Ni^{3+} (Fig. 2b). The fitted peaks at 852.3 eV and 872.9 eV correspond to Ni^{2+}. The binding energy of Ni^{3+} corresponds to 855.6 eV and 874.3 eV.[26] For Co 2p (Fig. 2c), the peaks of Co^{2+} are located at binding energies of 780.9 eV and 797.9 eV, while the binding energies at 776.3 eV and 796.5 eV suggest the presence of Co^{3+}.[27] In the S 2p spectra (Fig. 2d), the peaks at 163.4 eV and 161.9 eV correspond to S $2p_{1/2}$ and S $2p_{3/2}$, respectively.[28] Fig. 2e shows the O 1s spectra. The binding energy at 530.4 eV belongs to a metal–oxygen bond, while the peak at 531.2 eV is associated with hydroxide and the O_3 at 532.2 eV represents adsorbed water.[29] The C 1s spectrum can be divided into 284.7 eV (C–C/C═C), 285.9 eV (C–O/C–S) and 288.6 eV (O–C═O) (Fig. 2f).[30]

Fig. 3a shows the SEM image of the $NiCo_2S_4$ sample uniformly distributed on the nickel foam substrate. From the inset, the average thickness of the nanosheets is 10 nm. From the inset in Fig. 3b, high-magnification SEM images of the $NiCo_2S_4$@$Ni(OH)_2$-1 product indicate that the nanosheets intermingle with each other and form a petal-like structure. SEM images of the $NiCo_2S_4$@$Ni(OH)_2$-2 sample are presented in Fig. 3c. One finds that some nanosheets are assembled into nanoflower structures. The inset demonstrates that the nanoflower possesses a uniform shape. As the reaction time increases,

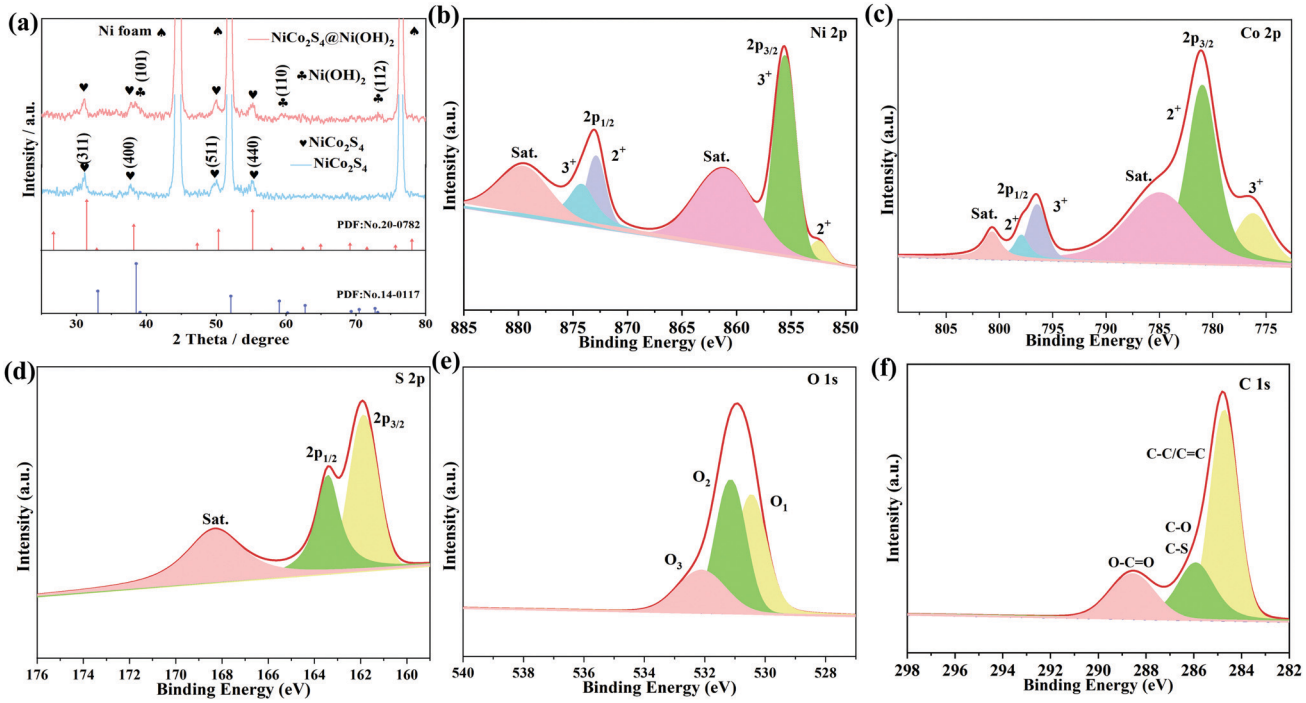

Fig. 2 Structural characterization: (a) XRD patterns, (b–f) XPS spectra.

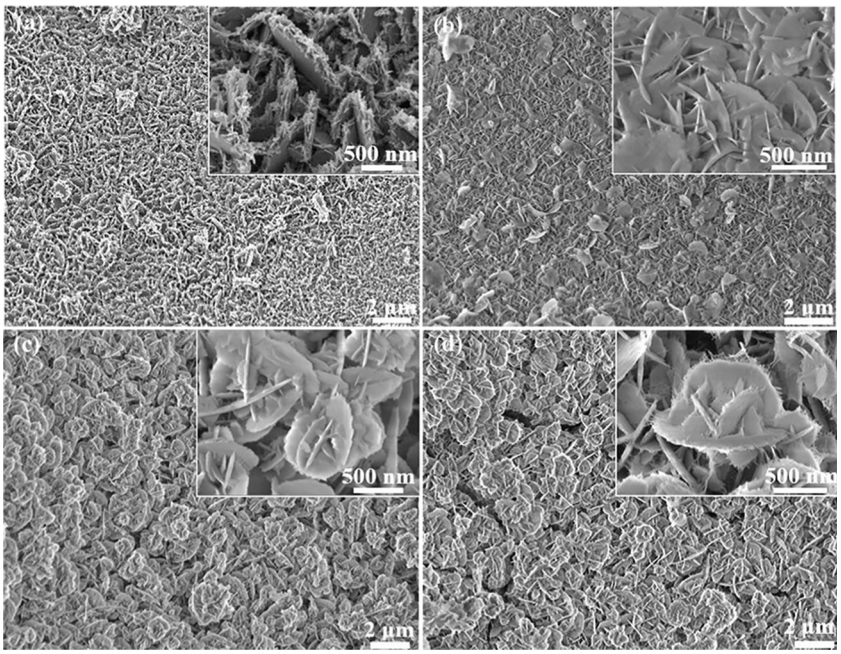

Fig. 3 SEM images of the samples: (a) $NiCo_2S_4$, (b) $NiCo_2S_4$@$Ni(OH)_2$-1, (c) $NiCo_2S_4$@$Ni(OH)_2$-2, (d) $NiCo_2S_4$@$Ni(OH)_2$-4.

the shape of the nanoflower remains constant while the thickness of the lamellae increases (Fig. 3d). As can be seen in the inset, the surface of the $NiCo_2S_4$@$Ni(OH)_2$-4 nanosheets is slightly rough.

Cyclic voltammetry curves of several samples at 20 mV s^{-1} are shown in Fig. 4a. The CV curve area of the $NiCo_2S_4$@$Ni(OH)_2$-2 product is much larger than those of the other materials, indicating its high capacity. Fig. 4b shows a comparison of the capacitance of several synthesized products, which also confirms that the hybrid structured samples present a high specific capacitance. When the current density is increased to 10 A g^{-1}, the capacitance retentions of the $NiCo_2S_4$, $NiCo_2S_4$@$Ni(OH)_2$-1, $NiCo_2S_4$@$Ni(OH)_2$-2 and $NiCo_2S_4$@$Ni(OH)_2$-4 electrode materials

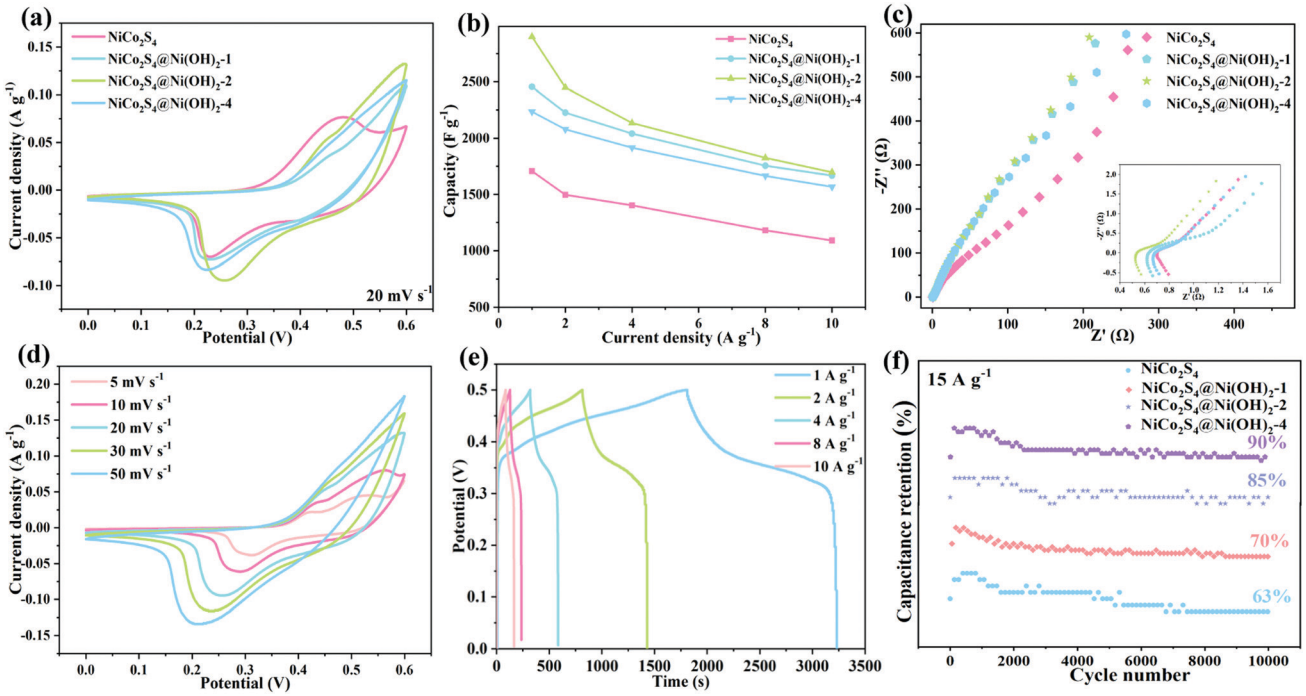

Fig. 4 Electrochemical characterization: (a) cyclic voltammetry curves, (b) galvanostatic charge–discharge curves, (c) Nyquist plots, (d) cyclic voltammetry curves of an $NiCo_2S_4$@$Ni(OH)_2$-2 nanosheet, (e) galvanostatic charge–discharge curves of $NiCo_2S_4$@$Ni(OH)_2$-2 samples, (f) cycling performance.

are 63.88%, 67.93%, 58.53% and 70.11%, respectively. To further understand the electrochemical kinetics of the electrode materials, tests of their electrochemical impedance were conducted, as shown in Fig. 4c. The intersection with the real axis represents the equivalent resistance (R_s). R_s values of the samples are 0.79, 0.66, 0.57 and 0.71 Ω, respectively. Among them, the R_s value of the $NiCo_2S_4$@$Ni(OH)_2$-2 product is the smallest. In addition, the $NiCo_2S_4$@$Ni(OH)_2$-2 electrode material shows a small semicircle in the high-frequency region and a large slope in the low-frequency one. It demonstrates fast

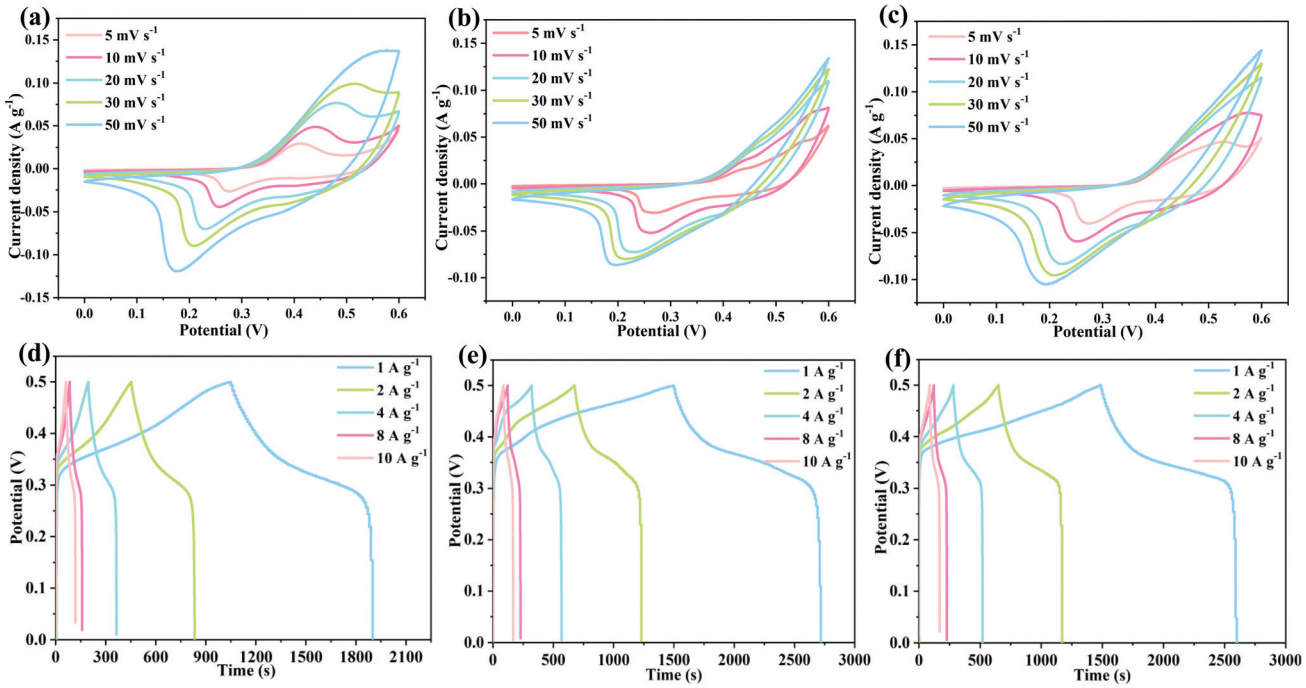

Fig. 5 Electrochemical performance of the electrode materials: (a–c) cyclic voltammetry curves, (d–f) galvanostatic charge–discharge curves.

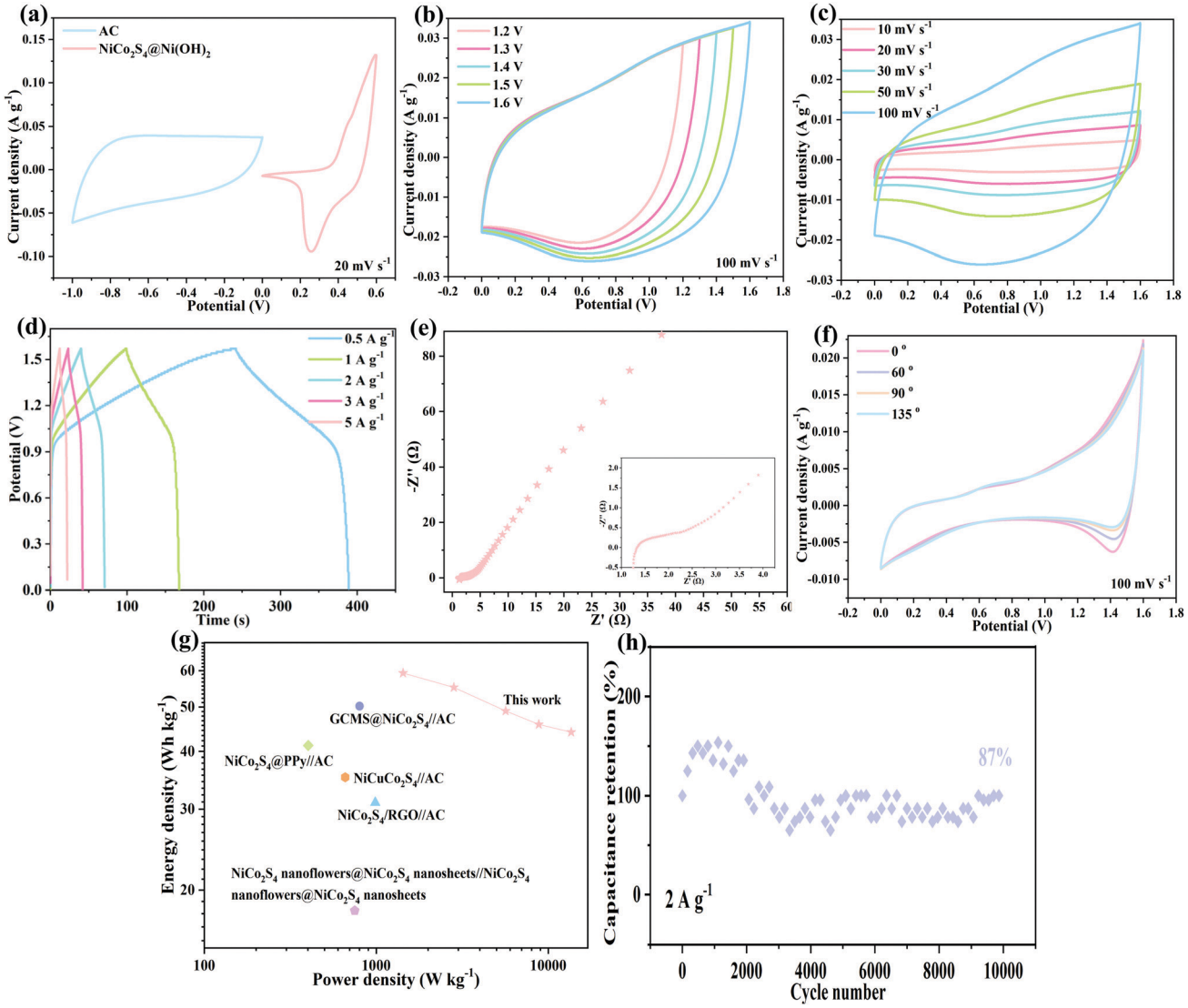

Fig. 6 Electrochemical characterization of the device: (a) CV curves, (b) CV curves at different voltage windows, (c) CV curves at various scanning rates, (d) GCD curves, (e) Nyquist plot, (f) CV curves at different bending angles, (g) Ragone plot, (h) cycling performance.

electron transport kinetics and ion diffusion rates at the electrode/electrolyte interface.[31,32]

Fig. 4d shows cyclic voltammetry curves of $NiCo_2S_4$@$Ni(OH)_2$-2 at different scan rates. Obvious redox peaks can be observed, which are mainly reversible reactions of the Ni^{2+}/Ni^{3+} and Co^{2+}/Co^{3+} redox pairs.[33] As the scan rate increases from 5 m V s^{-1} to 50 mV s^{-1}, the cyclic voltammetry curve slopes and the redox peaks shift in opposite directions, The results show that the migration speed of electrolyte ions increases with an increase in scan rate at the interface.[34] A plateau can be observed in the galvanostatic charge–discharge (GCD) curve at 1 to 10 A g^{-1} (Fig. 4e), indicating their pseudocapacitive behaviors. From the GCD curves, the value of the mass capacitance (C) can be calculated from the following equation:

$$C = I\Delta t/m\Delta V \quad (2)$$

I, Δt, m and ΔV represent current density, discharge time, the loading mass of the active material and voltage window, respectively. The calculated specific capacitances are 2899.48 F g^{-1} (1 A g^{-1}), 2448.92 F g^{-1} (2 A g^{-1}), 2135.84 F g^{-1} (4 A g^{-1}), 1825.71 F g^{-1} (8 A g^{-1}) and 1697.00 F g^{-1} (10 A g^{-1}). Fig. 4f shows the cycling property of several electrode materials. The $NiCo_2S_4$@$Ni(OH)_2$-2 sample was tested for 10 000 cycles at 15 A g^{-1} and it retained 85% of the initial capacitance. The $NiCo_2S_4$, $NiCo_2S_4$@$Ni(OH)_2$-1 and $NiCo_2S_4$@$Ni(OH)_2$-4 electrode materials showed capacitance retentions of 63%, 70% and 90%, respectively.

Cyclic voltammetry curves of several samples are shown in Fig. 5(a–c). When the scanning speed is increased, the shapes of the curves are well preserved, suggesting their excellent rate characteristics. Furthermore, as shown in Fig. 5(d–f), the mass capacitances of the three samples are 1707.84, 2455.17 and 2235.74 F g^{-1} at 1 A g^{-1}, respectively. The redox reactions can be described as follows:[35]

$$NiCo_2S_4 + 2OH^- = NiSOH + CoSOH + 2e^- \quad (3)$$

$$NiSOH + OH^- = NiSO + H_2O + e^- \quad (4)$$

$$CoSOH + OH^- = CoSO + H_2O + e^- \quad (5)$$

$$Ni(OH)_2 + OH^- = NiOOH + H_2O + e^- \quad (6)$$

To further explore the practical applications of the synthesised product, an asymmetric capacitor was assembled. Fig. 6a shows the CV curves at 20 mV s^{-1}. The operating voltage range of activated carbon is −1.0 to 0 V and that of the $NiCo_2S_4$@$Ni(OH)_2$-2 sample is 0 to 0.6 V. Based on a combination of the voltage windows of activated carbon and the $NiCo_2S_4$@$Ni(OH)_2$-2 product, the assembled asymmetric device can operate stably in a voltage window of 1.6 V. The CV curves at different voltage windows indicate that the device can still operate stably at 1.6 V.[36,37] From the CV curves of the devices at scan rates of 10 to 100 mV s^{-1} (Fig. 6c), the specific capacitance of the hybrid device is mainly composed of the double layer capacitance of the activated carbon and the pseudocapacitance of the $NiCo_2S_4$@$Ni(OH)_2$-2 electrode material.[38,39] Galvanostatic charge–discharge curves at different current densities are shown in Fig. 6d. The specific capacitances are 48.08, 44.75, 39.77, 37.17 and 35.75 F g^{-1} at 0.5, 1, 2, 3, and 5 A g^{-1}, respectively. The electrochemical behaviour of the asymmetric device was further determined by electrochemical impedance spectroscopy, as shown in Fig. 6e. The equivalent resistance is 1.24 Ω. The small semicircle and large slope indicate its low resistance.

In addition, the mechanical stability of the assembled device was also investigated. Fig. 6f shows the cyclic voltammetry curves bending from 0° to 135°. They show a similar shape and the enclosed area remains unchanged, demonstrating the excellent mechanical flexibility.[40] The corresponding energy density (E) and power density (P) can be derived based on the following equations:

$$E = 1/2CV^2 \quad (7)$$

$$P = E/\Delta t \quad (8)$$

where C is specific capacitance, V refers to voltage window, and Δt represents discharge time. Fig. 6g shows a Ragone plot of several devices, where the power density of our device is 1432.07 W kg^{-1}, which is better than some literature reports.[24,41–44] Finally, the cycling performance of the device was investigated at 2 A g^{-1}, as shown in Fig. 6h. It was found that the capacitance retention could still reach 87% after 10 000 cycles.

4. Conclusions

In summary, we have synthesized several hybrid-structured $NiCo_2S_4$@$Ni(OH)_2$ samples by a multi-step hydrothermal route. The results show that nickel atoms increase the energy density of the material, while cobalt both stabilizes the layered structure of the material and improves its cycling stability and rate properties. It improves the electrical conductivity and electronic transfer rate of the hybrid samples. The $NiCo_2S_4$@$Ni(OH)_2$-2 product delivers a high specific capacitance. The hybrid device shows outstanding cycle stability and mechanical flexibility. This suggests that the obtained composite electrodes could be potential candidates for future energy storage devices.

Conflicts of interest

There are no conflicts to declare.

References

1 M. Z. Dai, D. P. Zhao and X. Wu, *Chin. Chem. Lett.*, 2020, **31**, 2177–2188.
2 D. P. Zhao, R. Zhang, M. Z. Dai, H. Q. Liu, W. Jian, F. Q. Bai and X. Wu, *Small*, 2022, **18**, 2107268.
3 C. K. Luo, L. Xiao and X. Wu, *Mater. Adv.*, 2022, **3**, 604–610.
4 Y. Liu and X. Wu, *Nano Energy*, 2021, **86**, 106124.
5 X. Y. Xu, T. Wei, R. Xiong, Z. N. Zhang, X. J. Zhang, S. L. Qiao, Q. Li and Y. Q. Hu, *Surf. Coat. Technol.*, 2021, **413**, 127085.
6 C. Liu and X. Wu, *Chem. Eng. J.*, 2020, **392**, 123651.
7 Q. Xia, T. Xia and X. Wu, *Rare Met.*, 2022, **41**, 1195–1201.
8 S. G. Dai, Y. C. Bai, W. X. Shen, S. Zhang, H. Hu, J. W. Fu, X. C. Wang, C. G. Hu and M. L. Liu, *J. Power Sources*, 2021, **482**, 228915.
9 X. Y. Liang, H. He, X. J. Yang, W. Lü, L. Y. Wang and X. S. Li, *J. Energy Storage*, 2021, **42**, 103105.
10 Y. D. Dong, L. Xing, F. Hu, A. Umar and X. Wu, *Mater. Res. Bull.*, 2018, **107**, 391–396.
11 C. Y. Liu, H. L. Wang, X. C. Zhao, H. L. Liu, Y. W. Sun, L. Tao, M. H. Huang, J. Shi and Z. C. Shi, *J. Power Sources*, 2020, **457**, 228056.
12 X. J. Tan, Z. X. Duan, H. Q. Liu, X. Wu and Y. R. Cho, *Mater. Res. Bull.*, 2022, **146**, 111626.
13 Z. G. Zou, Q. Wang, J. Yan, K. Zhu, K. Ye, G. L. Wang and D. X. Cao, *ACS Nano*, 2021, **15**, 12140–12150.
14 Y. C. Ye, X. Guo, Y. J. Ma, Q. Zhao, Y. Sui, J. Song, W. J. Ma, P. X. Zhang and C. L. Qin, *J. Electroanal. Chem.*, 2021, **897**, 115588.
15 Z. Q. Ma, Z. Q. Sun, H. Jiang, F. Z. Li, Q. Wang and F. Y. Qu, *Appl. Surf. Sci.*, 2020, **533**, 147521.
16 T. Xia, Y. Liu, M. Z. Dai, Q. Xia and X. Wu, *Dalton Trans.*, 2021, **50**, 4045–4052.
17 Y. F. Yang, D. Cheng, S. J. Chen, Y. L. Guan and J. Xiong, *Electrochim. Acta*, 2016, **193**, 116–127.
18 M. Z. Dai, H. Q. Liu, D. P. Zhao, X. F. Zhu, A. Umar, H. Algarni and X. Wu, *ACS Appl. Nano Mater.*, 2021, **4**, 5461–5468.
19 W. H. Yang, H. Guo, T. Fan, X. Zhao, L. W. Zhang, Q. X. Guan, N. Wu, Y. J. Cao and W. Yang, *Colloids Surf., A*, 2021, **615**, 126178.
20 A. Sharifi, M. J. Arvand and S. Daneshvar, *J. Alloys Compd.*, 2021, **856**, 158101.
21 H. Q. Liu, D. P. Zhao, Y. Liu, Y. L. Tong, X. Wu and G. Z. Shen, *Sci. China Mater.*, 2021, **64**, 581–591.

22 R. Andaveh, G. B. Darband, M. Maleki and A. S. Rouhaghdam, *J. Mater. Chem. A*, 2022, **10**, 5147–5173.
23 X. Yang, Y. W. Yao, Q. Wang, K. Zhu, K. Ye, G. L. Wang, D. X. Cao and J. Yan, *Adv. Funct. Mater.*, 2022, **32**, 2109479.
24 J. Li, Y. J. Zou, B. Li, F. Xu, H. L. Chu, S. J. Qiu, J. Zhang, L. X. Sun and C. L. Xiang, *Ceram. Int.*, 2021, **47**, 16562–16569.
25 K. Sekar, G. Raji, S. Y. Chen, S. H. Liu and R. M. Xing, *Appl. Surf. Sci.*, 2020, **527**, 146856.
26 Y. X. Zeng, Y. Meng, Z. Z. Lai, X. Y. Zhang, M. H. Yu, P. P. Fang, M. M. Wu, Y. X. Tong and X. H. Lu, *Adv. Mater.*, 2017, **29**, 1702698.
27 Y. Z. Lu, J. Wang, S. Q. Zeng, L. J. Zhou, W. Xu, D. Z. Zheng, J. Liu, Y. X. Zeng and X. H. Lu, *J. Mater. Chem. A*, 2019, **7**, 21678–21683.
28 S. Kumar, S. Sekar, A. K. Kaliamurthy and S. Lee, *J. Mater. Res. Technol.*, 2021, **12**, 2489–2501.
29 D. K. Jiang, M. J. Zheng, Y. X. You, F. G. Li, H. Yuan, W. L. Zhang, L. Ma and W. Z. Shen, *J. Alloys Compd.*, 2021, **875**, 159929.
30 W. B. Guo, Z. F. Cong, Z. H. Guo, P. P. Zhang, Y. H. Chen, W. G. Hu, Z. L. Wang and X. Pu, *Adv. Funct. Mater.*, 2021, **31**, 2104348.
31 C. Liu and X. Wu, *Mater. Res. Bull.*, 2018, **103**, 55–62.
32 Y. X. Zeng, Z. Z. Lai, Y. Han, H. Z. Zhang, S. L. Xie and X. H. Lu, *Adv. Mater.*, 2018, **30**, 1802396.
33 X. Y. Yang, C. L. Xiang, Y. J. Zou, F. Xu, X. Q. Mao, X. B. Hu, J. Zhang and L. X. Sun, *J. Mater. Res. Technol.*, 2020, **9**, 13718–13728.
34 K. Thompson, J. Choi, D. Neupane, S. R. Mishra, F. Perez and R. K. Gupta, *Surf. Coat. Technol.*, 2021, **421**, 127435.
35 B. B. Shi, B. Saravanakumar, W. Wei, G. P. Dong, S. J. Wu, X. B. Lu, M. Zeng, X. S. Gao, Q. M. Wang, G. F. Zhou, J. M. Liu, K. Kempa and J. W. Gao, *J. Alloys Compd.*, 2019, **790**, 693–702.
36 N. Liu, Z. H. Pan, X. Y. Ding, J. Yang, G. G. Xu, L. G. Li, Q. Wang, M. N. Liu and Y. G. Zhang, *J. Energy Chem.*, 2020, **41**, 209–215.
37 S. Wang, P. Zhang and C. Liu, *Colloids Surf., A*, 2021, **616**, 126334.
38 G. T. Xiang, Y. Meng, G. M. Qu, J. M. Yin, B. Teng, Q. Wei and X. J. Xu, *Sci. Bull.*, 2020, **65**, 443–451.
39 W. Y. Chen, X. M. Zhang, L. Mo, Y. S. Zhang, S. H. Chen, X. X. Zhang and L. H. Hu, *Chem. Eng. J.*, 2020, **388**, 124109.
40 B. Xu, H. B. Zhang, H. Mei and D. F. Sun, *Coord. Chem. Rev.*, 2020, **420**, 213438.
41 W. L. Wu, C. H. Zhao, C. W. Wang, T. T. Liu, L. Wang and J. F. Zhu, *Appl. Surf. Sci.*, 2021, **563**, 150324.
42 S. K. Shinde, H. M. Yadav, G. S. Ghodake, A. D. Jagadale, M. B. Jalak and D. Y. Kim, *Ceram. Int.*, 2021, **47**, 15639–15647.
43 X. B. Chen, B. X. Ding and Y. T. Sun, *J. Energy Storage*, 2021, **35**, 102309.
44 H. I. Hsiang, C. H. She and S. H. Chung, *Ceram. Int.*, 2021, **47**, 25942–25950.